Spanning spatial scales with functional imaging in the human brain; initial experiences at 10.5 Tesla

Luca Vizioli[1], Steen Moeller[1], Logan Dowdle[1,3], Andrea Grant[1], Alireza Sadeghi-Tarakameh[1], Yigitcan Eryaman[1], Russel L. Lagore R[1], Edward Auerbach[1], Gregor Adriany[1], Lasse Knudsen[2], Federico De Martino[3], Lonike Faes[3], Essa Yacoub[1], Kamil Uğurbil[1]

1. Center for Magnetic Resonance Research (CMRR), University of Minnesota, Minneapolis, MN 55455

2. Aarhus University, Center of Functionally Integrative Neuroscience, Building 1710, Universitetsbyen 3, 8000 Aarhus, Denmark

3. Department of Cognitive Neuroscience, Maastricht University, Maastricht, Universiteitssingel 40, 6229 ER Maastricht, Netherlands

ABSTRACT

One of the most important new frontiers in the effort to improve the spatial resolution and accuracy of imaging of human brain activity is the recent development of greater than 10 Tesla magnetic fields. Here we present initial results for 10.5 Tesla Blood Oxygenation Level Dependent (BOLD) based functional brain imaging (fMRI) of the human brain acquired with previously unavailable or difficult to attain spatial resolutions and functional contrast. We present data obtained with nominal isotropic resolutions ranging from 0.65 to 0.35 mm for partial brain coverage for stimulus evoked responses, and 0.75 mm for whole brain coverage to capture the spontaneous fluctuations that are the source of functional connectivity measures. The increasingly higher nominal resolutions (i.e. smaller voxel volumes and dimensions) employed in image acquisition were shown to correspond to real gains in resolution using image reconstruction methods developed to minimize blurring. Existence of supralinear gains in stimulus-evoked percent signal change and major improvements in statistical significance were evident relative to 7 Tesla, the most advanced commercially available ultrahigh magnetic field platform currently employed in human brain studies. These results were feasible due to gains in intrinsic signal-to-noise ratio, BOLD contrast, and image acceleration provided by the uniquely high magnetic field of 10.5 Tesla, and the use of novel high channel count arrays to capture these gains. The results provide a preview of the potential that will be available in the new era of greater than 10 Tesla human functional imaging, particularly for mesoscale functional organizations and connectivity.

1. INTRODUCTION

Following its introduction in the early 90s[1,2], functional MRI (fMRI) based on the Blood Oxygen Level Dependent (BOLD) contrast has rapidly emerged as the most powerful and widely used noninvasive tool for studying the human brain. Nevertheless, like all techniques at our disposal for studying the brain, fMRI had and still has limitations, particularly with respect to spatiotemporal resolution and the fidelity of the functional maps relative to the neuronal activity that induces them. Overcoming these limitations has been a major research focus since the introduction of the method, and in this effort, the development of ultrahigh magnetic field of 7 Tesla [3,4] was one of, if not the most, consequential initiative.

The brain operates over a vast spatial scale, going from the cellular level to mesoscopic scale neuronal ensembles, and to networks involving billions of neurons distributed over large parts of the brain, if not the entire brain. However, at 2 mm isotropic resolution, which would represent the high end of the resolutions employed in the vast majority of human fMRI experiments conducted at 3 Tesla, the fMRI voxel (the smallest volume unit that defines the spatial resolution of the image) is 2^3 mm^3 (i.e. 8 μL) in volume, containing more than a million neurons. Although many useful studies can be caried out at such a resolution, ultimately it is a coarse scale relative to the magnitude of the problem at hand. The development of 7T ushered in the ability to break this mm-resolution barrier and access mesoscale neuronal organizations with submillimeter resolutions (e.g., reviews [4-16]), starting with the demonstration of functional mapping of ocular dominance columns and orientations domains[17], and, in addition, provide higher detection sensitivity and model predictive power (e.g.,[18-20]) at any spatial resolution.

Recently popular 7T fMRI studies targeting differentiation of activity across cortical layers is also an example of such high resolution, mesoscale studies in the human brain. The ~1.5- to ~4-mm thick mammalian cortex is characterized by different cell types and connectivity organized across six different cortical layers, with bottom-up (i.e. feedforward) and top-down (i.e. feedback)

connections terminating in different laminae. Brain function relies on this architecture and layer-dependent computations that integrate feedforward, feedback and recursive circuital interactions. Perturbations in these processes have also been proposed as models of dysfunction underlying neuropsychiatric disorders[21,22]. Individualized perceptual impairments associated with Alzheimer's[23] , autism[24], and psychoses[25] – all of which are enormous societal burdens – are thought to ensue from faulty feedforward or feedback connections. Amyotrophic lateral sclerosis, a fatal neurodegenerative disease, is hypothesized to start with selective depletion neurons[26,27] in layer Vb of the motor cortex followed by a subsequent spread of pathology towards superficial layers[22]. Yet, the ability to access these layer-dependent computations and/or pathological developments robustly in the human brain with fMRI remains largely beyond current capabilities. For example, despite major advances in spatiotemporal sampling for whole brain fMRI and dMRI[28,29], the Human Connectome Project (HCP)[30,31] attained only ~1- to 8-μL voxel resolutions[28-30]. It was not possible to reach functional connectivity measures across different cortical layers, a capability that is considered essential for the next generation HCP initiatives[32]. With FOV restriction, 7T task/stimulus based fMRI has reached nominal voxel volumes of ~0.5 to 1 μL in the human brain (e.g., reviews[4-12,14-16]), demonstrating feasibility. However, signal- and contrast-to-noise ratios (SNR and fCNR respectively) and spatial resolution remain highly suboptimal. It was possible, for example, to demonstrate[33] the potential of distinguishing the input and output layers of the primary motor cortex (layers II/III and Vb/V, respectively[34]); however, the resolutions and magnitude of the effects were marginal for visualizing consistent layer differences (see Fig. 1.1 in [33]). Similarly, it was possible to map *axis of motion* features in the human MT with layer and column resolution but ***not*** the *direction of motion* subclusters that distinguish the motion in the two different directions along a given axis[35].

The afore-listed challenges were recognized in the first strategic plan developed for the first US BRAIN Initiative [36,37], which called for the fMRI method to achieve "*submillimeter spatial resolution"* in the human brain with an ambitious resolution target of ≤0.1-μL voxel volume. This

target was revised five years later to 0.01μL[38], emphasizing that though *"ambitious*" and *"elusive*", "*current data suggest that such a technological goal is worth achieving*"[38] with the aim of bridging the gap between non-invasive human neuroimaging and invasive electrophysiology and optical imaging methods. The goal is not just to demonstrate the feasibility of achieving such high resolutions; rather, it is to achieve it with high enough SNR and fCNR to make it a useful tool in the study of normal brain function and/or brain pathologies.

One of the most recent significant technological developments poised to make major contributions to meeting these challenges is human imaging at magnetic fields greater than 10T [39,40], exemplified by the 10.5T effort in our laboratory[41-49]. Having investigated and quantified the large SNR gains relevant for human brain imaging at this field strength[46-50] and developed novel radiofrequency arrays to capture these gains over the entire brain[48-50], we report for the first time initial efforts pushing the limits of functional imaging performance at this unique magnetic field strength. The data demonstrate the potential for unprecedented spatial resolutions and coverage, including across cortical regions, such as visual and auditory cortices, with a spatial precision that goes well beyond what has been typically employed at 7T.

2. RESULTS

Most commonly employed BOLD fMRI method is based on gradient recalled echo (GRE) Echoplanar (EPI) acquisition. This is the methodology employed in the work reported in this paper. Typically, GRE BOLD fMRI studies conducted at 7T employ $\gtrsim$ 1mm isotropic nominal resolutions for large or whole brain coverage and ~0.8mm isotropic nominal resolution (~0.5 μL voxel volume) for high resolution experiments conducted with highly-restricted brain coverage to probe mesoscale neuronal organization; "nominal" refers to the resolution specified for the data acquisition - the real voxel dimensions typically exceed that of the nominal resolution for a variety of reason. In this paper, all resolutions given are nominal and isotropic unless otherwise specified. We have previously demonstrated GRE BOLD fMRI at 10.5T at 0.8mm resolution in papers that

introduced advanced arrays for 10.5T brain imaging[48-50]. Here we demonstrate fMRI with partial brain coverage using 0.65mm, 0.4mm and 0.35mm (nominal) isotropic resolution (~0.275μL, 0.064 and 0.042μL voxel volumes, respectively) using the GRE BOLD approach, and whole brain fMRI with 0.75 mm isotropic resolution.

2.1. 0.65 mm isotropic resolution GRE BOLD EPI images in auditory cortex at 10.5T

The SNR available at 10.5T is compatible with 0.65 mm isotropic resolution fMRI within practical data acquisition times even without any post-acquisition denoising strategies. However, such an acquisition creates several challenges. One major challenge is to keep the echo time (TE) sufficiently short to achieve TE≈T2* so as to optimize the fCNR [51,52]. At very high magnetic fields where the T2* is short, this requires the use partial Fourier (pF) and/or high accelerations along the phase encoding direction. In this case, image reconstruction without significantly blurring the image becomes a problem. Therefore, we developed an off-line reconstruction algorithm to handle this problem.

We acquired functional images during auditory stimulation (Figure 1) (3D GRE EPI; 0.65 mm iso voxels; TE=16.6 ms; TR=81 ms; iPAT 4; pF=5/8; 52 Slices; VAT (Volume Acquisition Time)=4536 ms; FOV (272x276mm) during a block auditory stimulation paradigm (see Methods). Although the EPI technique gets more challenging with increasing magnetic fields, high accelerations possible with the synergistic use of high magnetic fields with high channel count arrays[48,49] produce excellent quality EPI images at 10.5T, as demonstrated previously for 0.8 mm isotropic resolution[48,49], and illustrated for the 0.65mm resolution data in Figure 1a and 1b. Images were reconstructed and evaluated using 3 different strategies: 1) The vendor default reconstruction, which uses zero-padding to fill in the missing phase encode lines in k-space due to the partial Fourier (pF) acquisition, 2) Off-line reconstruction that uses Projection onto convex sets (POCS) [53] to fill in the missing lines in pF, and 3) POCS reconstruction followed by NORDIC denoising. Mean temporal SNR (tSNR) across voxels within the cortical ribbon (computes as the

mean across volumes of the preprocessed PSC (percent signal change) timecourses over their standard deviation) for the different image reconstructions were: 16.38 for zero-padded pF (std: 5.99), 10.54 for POCS pF (std: 4.06), and 23.31 for POCS pF with NORDIC (std: 11.41).

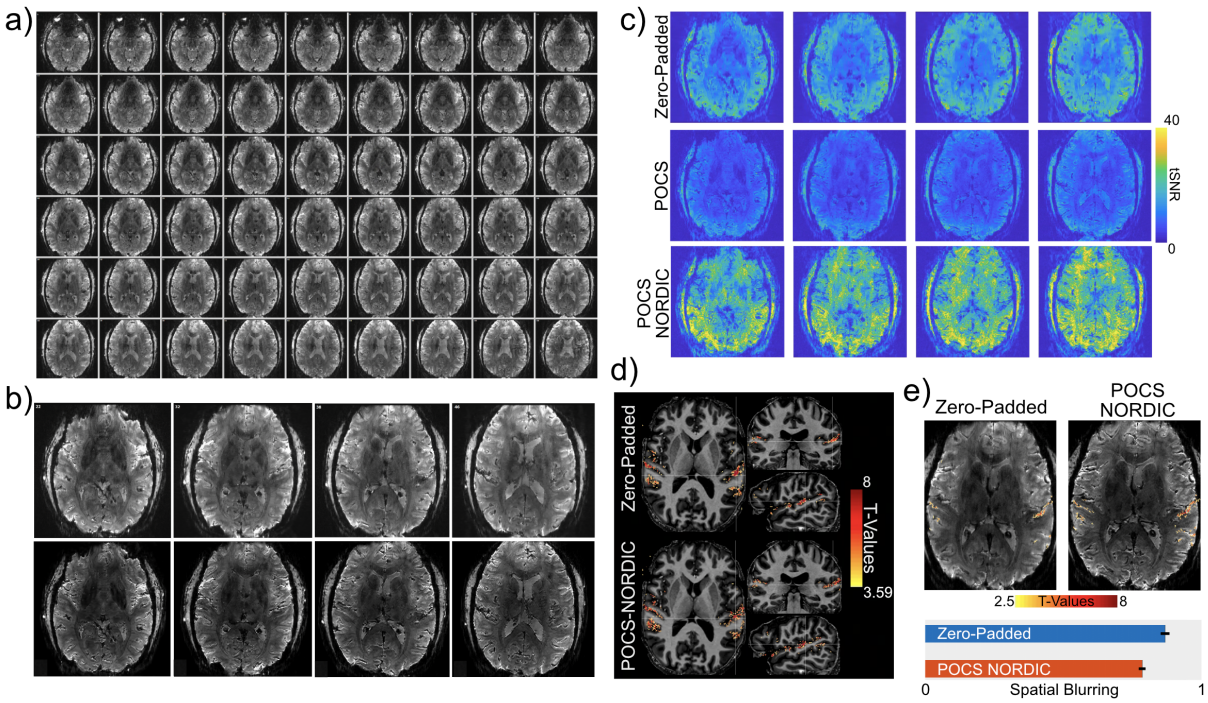

Figure1: 0.65 mm isotropic (nominal) resolution GRE BOLD fMRI with auditory stimulation. (a) Zero-Filled (online) Single image EPI slices showcasing the achievable coverage (i.e. all slices). (b) Zoom in on selected single slices of a single EPI volume for Zero-Filled (Dicoms) on the top and tailored offline recons on the bottom. (c) tSNR Maps for a single functional run after motion correction and linear detrending. (d) Activation to sounds (t-maps for sounds > 0) for 5 concatenated runs (just over 35 minutes of data) superimposed on a coregistered T1 (MP2RAGE) for Zero-Filled (Dicoms) on the top and POCS+NORDIC on the bottom. (e) Activation to sounds (t-maps for sounds > 0) for a single run superimposed on a single image EPI for Zero-Filled (Dicoms, left) POCS+NORDIC (right). The bottom plot of horizontal bars in blue and red in panel (e) show the average spatial blurring (i.e. autocorrelation in the GLM residuals) computed within the Grey Matter for 3 representative slices located towards the top, middle and bottom of the volume. The error bars show the standard error across 8 runs.

Functional maps with a t-threshold (t>3.59) and a cluster threshold of 4 voxels for the sounds>0 contrast across the auditory cortex are shown in Figure 1d for 5 runs concatenated for

zero-padded pF and POCS pF+NORDIC processing. Each run was approximately 8 min of data (i.e. 101 volumes). T-threshold was determined based on FDR correction (q<0.05) for the vendor default zero-padded data. We used the same t-threshold for the POCS NORDIC images (see [54]). Figure 1e shows the t-maps for the same t-contrast (sounds>0) for a single run of zero-padded and POCS+NORDIC images (p=0.01 uncorrected, and a voxel cluster threshold of 4).

To quantify spatial blurring beyond the "nominal" resolution specified in the functional maps and thus infer functional spatial precision, we estimated the global smoothness of individual EPI images in the fMRI time series using AFNI (3dFWHMx function)[55], for 3 representative slices within the cortical ribbon. The spatial autocorrelation was estimated using a Gaussian+monoexponential decay mixed model to account for possible long-tail autocorrelations. The FWHM from this mixed model estimate, averaged over 8 runs after data preprocessing (see Methods), was 0.95±0.009mm(ste) for the zero-padded and 0.86±0.0048mm(ste) for POCS+ NORDIC.

As expected, a t-test carried out across runs indicated that the zero-padded images were significantly smoother than the POCS pF+NORDIC ones ($t(7) = 15.72$; $p < 0.00001$). The SNR advantage that comes with this smoothness in the zero-filled pF processing was made up by the use of NORDIC for the POCS processed data. Figure 1c illustrates tSNR maps, demonstrating that indeed zero-padded vendor reconstruction has better tSNR compared to POCS alone, albeit with a compromised spatial resolution, but NORDIC improves the POCS reconstruction to yield the highest tSNR.

2.2. <u>0.4 mm isotropic resolution BOLD EPI images in visual cortex at 10.5T</u>

We recorded 0.4 mm nominal resolution (i.e. 0.064μL voxel volume) functional images in the same participant at 7T (3D GE EP ; iPAT3; 5/8 PF; 40 Slices; TR=111ms; VAT=4884ms; TE=24.2ms) and 10.5T (3D GE EPI; ;iPAT3; 5/8 PF; 40 Slices; TR=113; VAT=4972; TE=24.4) in a slab placed over the occipital cortex in the same subject (Figure 2). We used the same

experimental paradigm implemented in [54], consisting of a 24 seconds on/off block design with a center and a surround flickering checkerboard, with data acquired in consecutive but separate runs each of which was ~5 min. Data were processed with the vendor default reconstruction.

Figure 2a shows the activation maps for a single slice elicited by target and surround stimuli for a single run of 10.5T data before and after NORDIC denoising (respectively, center and

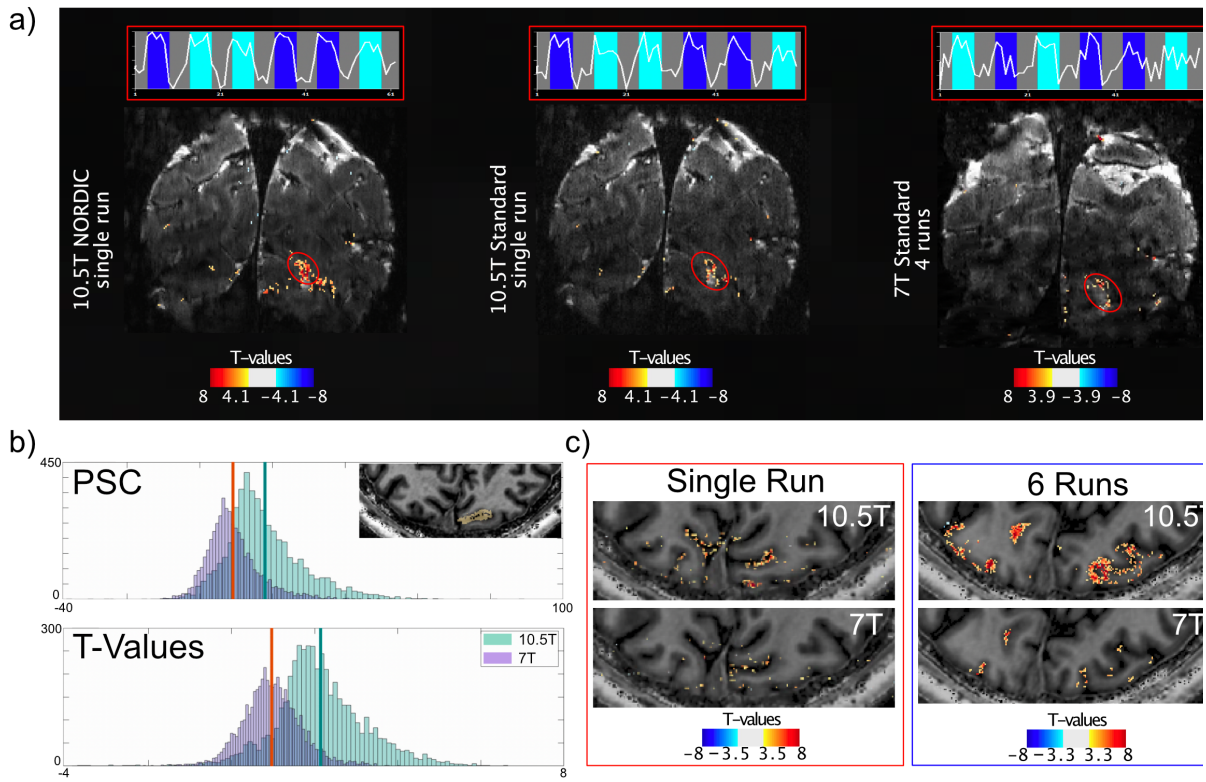

Figure 2: 0.4 mm isotropic functional imaging of retinotopically organized visual stimulation at 7T and 10.5T. (a) Activation maps (t-maps elicited by target and surround > 0) superimposed on a image EPI of a single slice obtained at 10.5T for a single run (approximately 5 minutes of data) before (leftmost) and after (middle) NORDIC denoising, and 4 runs (approximately 20 mins of data) of 7T data (rightmost); (b) Histograms for average (across 6 runs - i.e. 30 minutes of data) PSC (top) and T-values for the contrast Target and Surround >0 for all the voxels within the region of interested (show in the insert) computed by performing the overlap of the activation to 6 runs for 10.5T and 7T data. (c) 10.5T (top) and 7T (bottom) t-maps superimposed on a co-registered MP2RAGE image for the contrast target and surround >0, for a single run (left panel) and for 6 concatenated runs (right panel).

left most panels in Figure 2a) and for 4 concatenated runs of 7T data (right-most panel in Fig.2a). The voxels considered activated at the t-threshold (t>|8|) used are shown in color superimposed on a representative slice of a single EPI image encompassing V1. More specifically we show voxels that are significantly activated (q<.05, FDR corrected) for the t-contrast target ∩ surround > 0 for 20 minutes of 7T data (t(238) = 3.98; p=0.0001, where the number in the parenthesis (i.e. 238) is the degrees of freedom in the t-test)); versus 5 minutes of 10.5T data (t(57) = 4.1; p=0.0001), as well as a 10.5T NORDIC matched t-threshold. We also report the average timecourses for the 98 most active voxels for a single run within the retinotopic representation of target and surround. We further carried out a region of interest (ROI – see methods) analyses confined in the retinotopic representation of target and surround in V1(Figure 2b). Percent signal change (PSC) and T-values for the t-contrast target ∩ surround > 0 were computed independently per run and averaged across the 6 runs for the 10.5T and 7T images. The mean PSC across all voxels and runs within the ROI was 17.9351 (std across voxels: 1.7020) and 9.1769 (std across voxels: 1.5821) for the 10.5T and 7T images, respectively. The mean t-values across *all* voxels (i.e. irrespective of whether they are considered activated or not) and runs within the ROI was t(57) 2.1390 (std across voxels: 0.4) and t(58) 0.9691 (std across voxels: 0.14) for the 10.5T and 7T images, respectively. We also report the t-maps for the same t-contrast target ∩ surround > 0 for a single run (t>3.5) and for all 6 concatenated runs (t>3.3) of 7T and a single run of 10.5T data at the same t threshold (Figure 2c).

2.3. <u>0.35 mm isotropic BOLD EPI images in visual cortex:</u>

Figure 3 displays 0.35 isotropic (nominal) resolution images (0.0428 μL voxel volume; 3D GE EPI; 0.35 mm iso voxels; iPAT=4; 5/8 PF; 40 Slices; TR=104ms; VAT=5016ms; TE=22.6ms) over the visual cortex during the same target and surround block design visual paradigm used in Figure 2. Reconstruction employed our off-line algorithms.

Figure 3b and 3d shows the t-maps for the target (shown in red) >surround (shown in blue) contrast for 30 minutes of data (i.e. 6 functional runs) superimposed on a selection of slices from

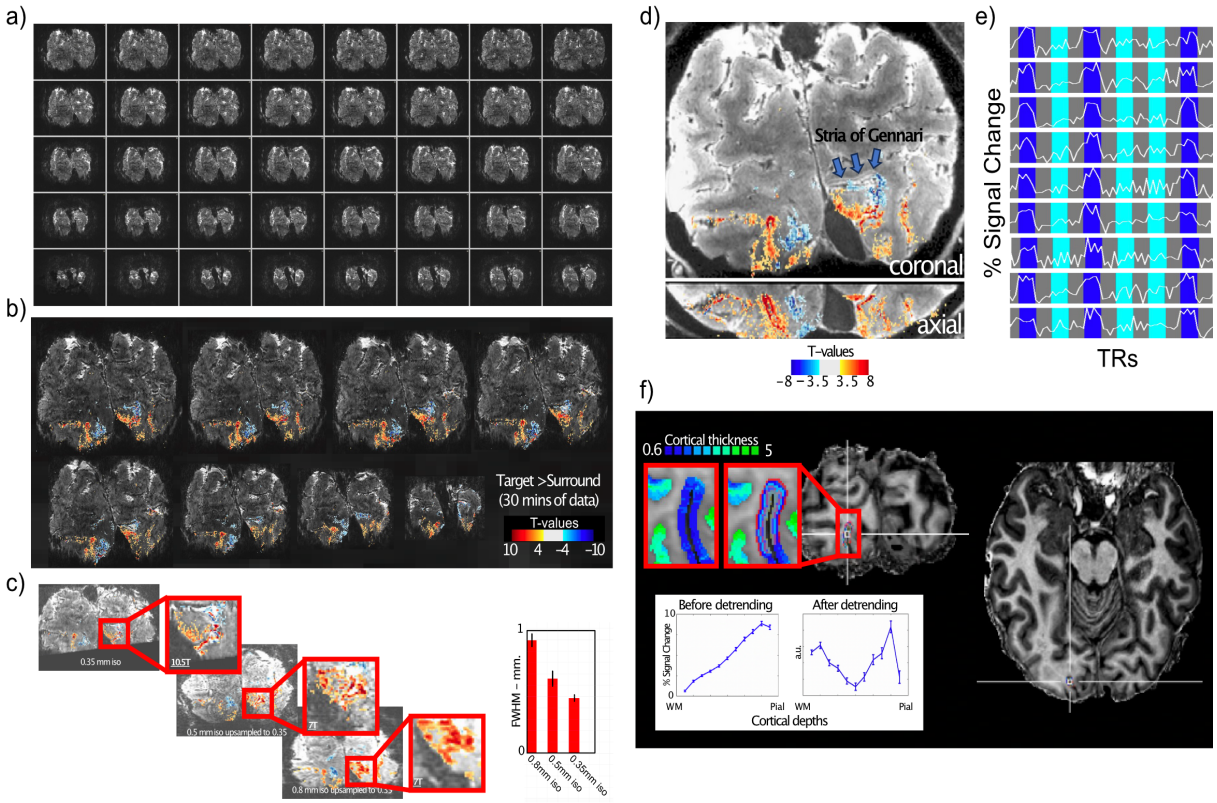

Figure 3. 0.35 mm resolution functional images at 10.5T. (a) Example of single volume EPI demonstrating coverage and image quality; (b) t-maps for the contrast target>surround superimposed on single slices EPI images; (c) Comparing target>surround t-Maps for 3 different resolutions. Maps are superimposed on single image EPI, zooming in on V1 (left) and estimated functional spatial blurring for each resolution (right). the 0.8 mm^3 and 0.5 mm^3 images were collected at 7T, while the 0.35 mm^3 data at 10.5T(d) target>surround T-Maps data superimposed on a T2* image; blue arrows indicate the Stria of Gennari (dark line); (e) examples of target selective single voxel single run timecourses. (f) cortical depths sampling. On the left we show the cortical depths superimposed on an axial slice of a coregistered MP2RAGE; no the top right we show the cortical thickness measurements on the same MP2RAGE, this time on coronal slices; bottom felt shows percent signal change across depths elicited by both surround and target condition in V2, before and after detrending to account for the typical GRE BOLD ramping profile (stemming from contamination or large draining vessels concentrated in proximity of the outer pial surface).

a single EPI volume and on the average of 2 co-registered T_2* weighted images from a multi-echo GRE acquisition (0.37mm whole brain, multi-echo GRE images. TEs: 4.07, 7.95, 11.83, 15.71, 19.59, 23.47, 27.35ms. TR 33ms, FA 10. 7/8ths partial Fourier. GRAPPA: 3x3 Matrix 576x576mm. 320 slices.), respectively. In Figure 3e we also report single voxel time courses for a single run for target specific voxels displaying all expected temporal hemodynamic characteristics (i.e. peaking during target blocks identified in the time course shown in Figure 3e in dark blue while the blocks where the surround stimuli was shown is in cyan).

2.4. Impact of blurring in isotropic 0.35mm, 0.5mm, 0.8mm resolution fMRI.

We compared functional blurring across 3 resolutions and two magnetic fields (Figure 3c). Specifically, using the same visual stimulation paradigm from the 0.35 mm 10.5T acquisitions, we recorded 0.8mm and 0.5mm resolution 7T GRE BOLD fMRI data in the same participant and estimated the global smoothness of individual EPI images in the fMRI time series using AFNI (3dFWHMx function)[55]. The effective resolution estimates were 0.49±0.006mm for the 10.5T 0.35 mm data, 0.65±0.049mm and 0.89±0.01mm for the 7T 0.5mm and 0.8mm data. t-test carried out across runs showed that the 10.5T 0.35 mm data were significantly less smooth than the 7T 0.5mm and the 0.8mm (2-sample T-test 0.35 vs 0.5mm: $p< 0.001$; vs 0.8mm: $p<0.001$).

We further performed cortical depth segmentation using an equivolume approach in BrainVoyager to segment the cortical ribbon into 11 depths (see methods) in V2 and extracted the average PSC within depth elicited by both stimuli (Figure 3f). Evoked PSC exhibited the typical ramping profile of GE BOLD, with increased amplitudes in proximity to the pial surface. After removing the linear trends associated with the venous contaminations on the BOLD signal we observed larger activation in inner and outer depths, relative to the middle depths (Figure 3f).

2.5. Whole brain fMRI with 0.75mm resolution BOLD EPI

The data presented so far was obtained with 3D GRE EPI with single shot for kx-ky and fully segmented acquisition for kz because of expected SNR advantages relative to slice based acquisition. However, it leads to long volume acquisition times (VAT) for large FOVs.

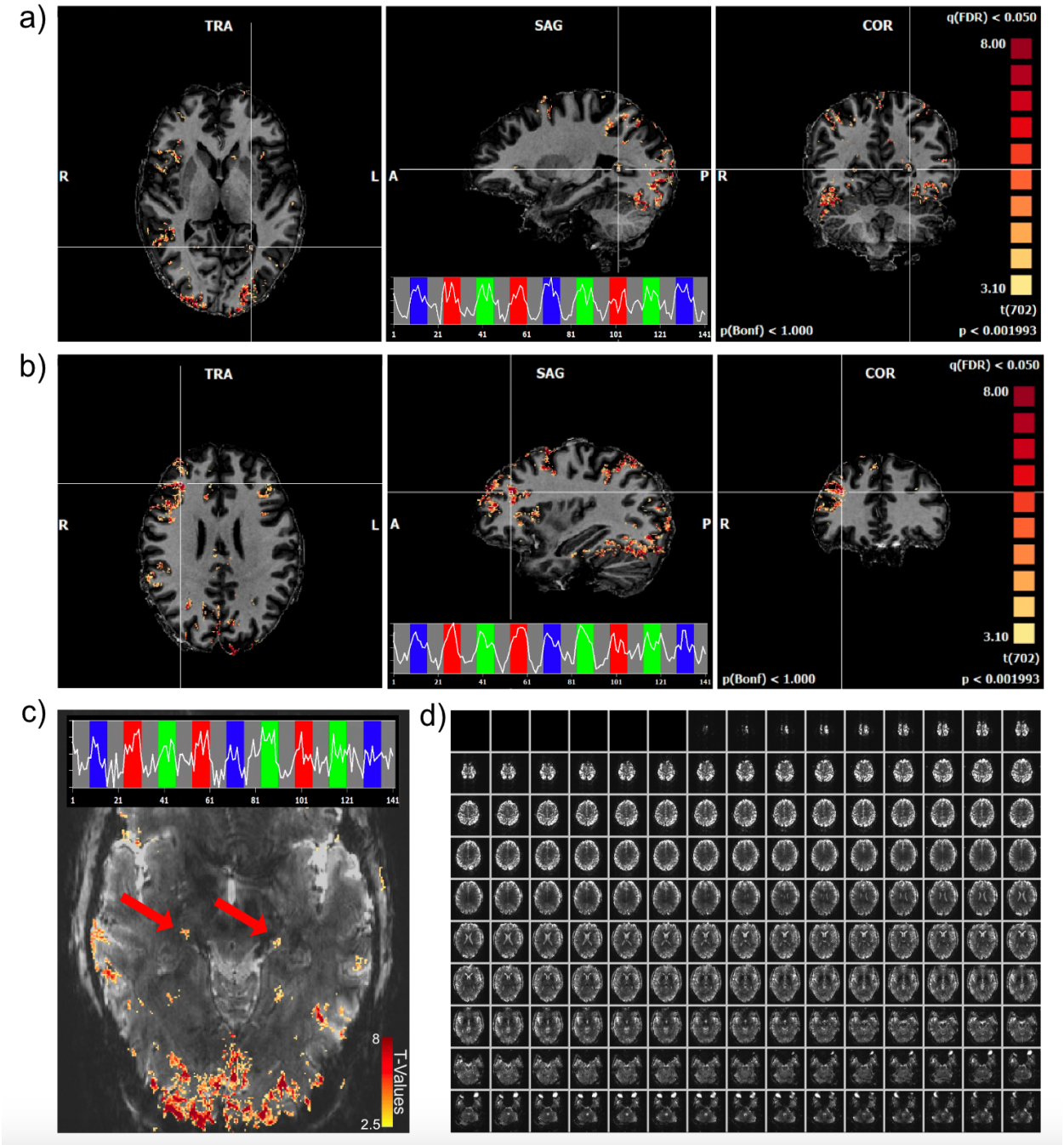

Figure 4: 0.75 mm isotropic whole brain fMRI activation (t-maps) elicited by object, bodies and faces > 0 for approximately 37 minutes of data. (a) and (b) show activation maps in two different sets of three orthogonal slices (superimposed on a co-registered MP2RAGE images) selected to show activation in the posterior cingulate cortex (a) and prefrontal cortex (b). The time-courses averaged for all voxels in the cluster identified by the cross-hairs are shown for a single ~9 min run in the middle panel of both Figure 4a and 4b. (c) activation in bilateral LGN (red arrows) after 2 voxel smoothing superimposed on a single image EPI and related time-course in a single run. (d) Single slice EPI images for the whole volume.

As such, the data presented in Figures 1 though 3 all used partial brain coverage, the extend of coverage decreasing with higher resolutions. For whole brain coverage, Slice (SMS)/Multiband approach[56-58] provides advantages for minimizing the volume acquisition time. As previously mentioned, 7T whole brain studies typically use spatial resolution of >1 mm isotropic nominal resolutions. Here, we report whole brain functional images using a 0.75 mm isotropic (i.e. 0.42μL) using SMS/MB GRE EPI acquisition with a temporal resolution (TR) of ~3.2 seconds (VAT is equal to TR in a 2D acquisition) (Figure 4). The acquisition parameters were: 0.75 mm iso voxels; iPAT=4; MB=3; 5/8 PF; 144 Slices; TR=3210ms; T= 17.8). We used a 24 seconds on/off block design visual paradigm. In this case, image acquisition and reconstruction was performed using the HCP Multiband reconstruction developed in CMRR (downloadable from https://www.cmrr.umn.edu/multiband/) *without denoising* and with minimal preprocessing (see Methods). Figure 4 shows the activation maps elicited by objects, bodies and faces within 37 minutes of data (i.e. 4 runs x ~9 min/run). Specifically, in panel 4a and 4b we report the voxels that were significantly active above baseline for the t-contrast faces $\cap$ bodies $\cap$ objects > 0 ($t(702)=3.10$; $q<0.05$ FDR corrected), superimposed on a co-registered T1 weighted MP2RAGE[59] anatomical reference. Figure 4a shows statistically significant activation in the posterior cingulate cortex. The related time-course for a single run (~9 min) is shown as an insert in the middle panel of Figure 4a; the time course was averaged across all voxels under the crosshair. Figure 4b shows a statistically significant activated in different slices than those shown in Figure 4a; these slices were selected to illustrate activation in the prefrontal cortex and the related time-course for a single run, averaged across all voxels under the crosshair. By decreasing the t-threshold to $t(702)=2.5$ ($p=0.012$ uncorrected) we can detect activation bilaterally in the LGN (Figure 1c). The related single run time-course reflects the average of all significantly active voxels for the left LGN only.

2.6. Quantitative T2 measurements*

Multi-Echo GRE sequences were used in the same human subject to obtain measurements of whole brain T2* at 0.37 mm (2 runs, 7 echoes, 4.07 – 27.35ms) and 0.8 mm (3 runs, 7 echoes, 4 – 28ms) isotropic resolutions at 10.5T, as well as a partial field of view acquisition (axial slab, centered around calcarine fissure) at a resolution of 0.35mm at 7T (6 runs,

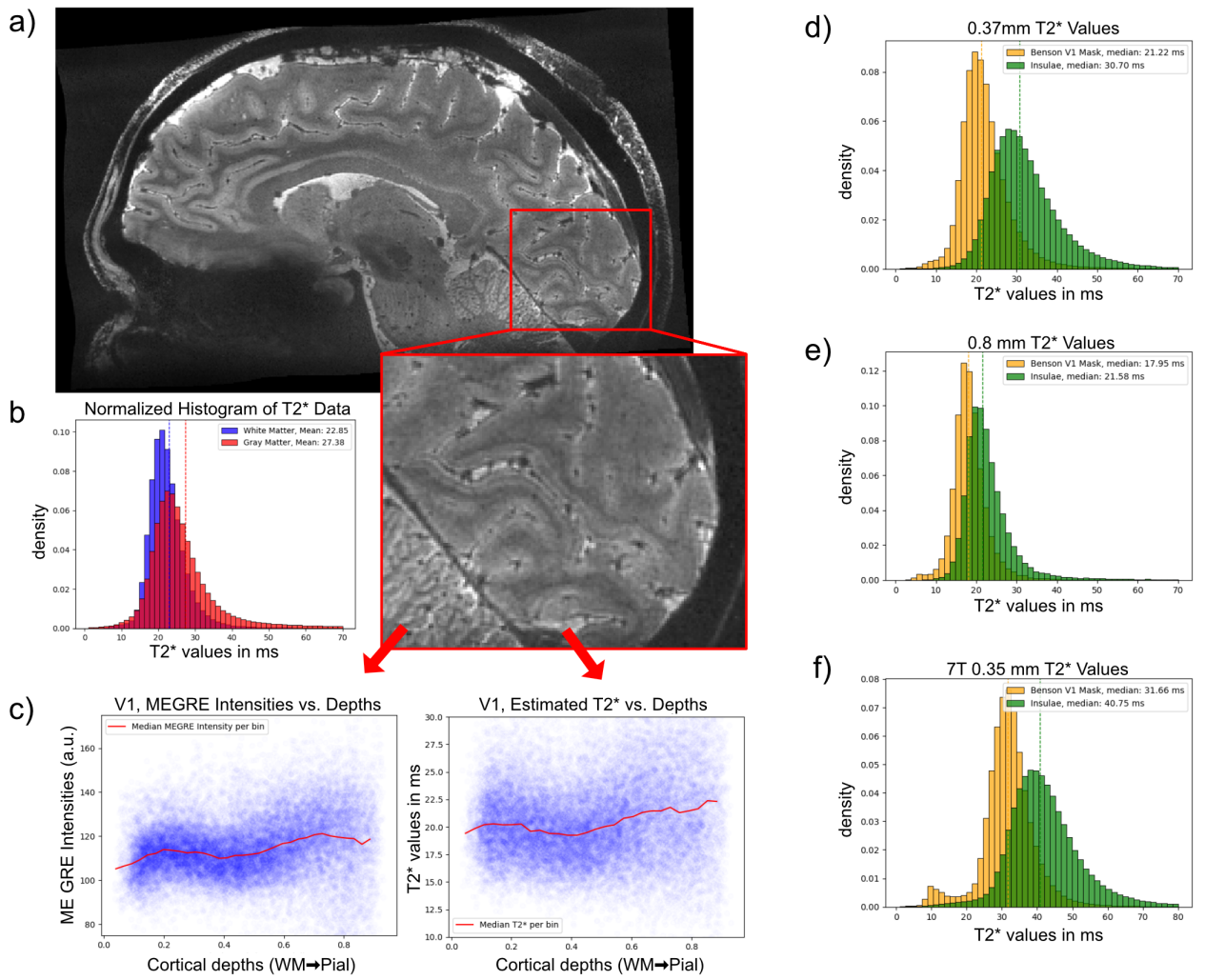

Figure 5: Quantitative T2* measurements at 10.5T (panels through e) and 7T (panel f). a) average of 2 ME GRE runs acquired a 10.5T with a spatial resolution of 0.37mm^3, zooming in on the calcarine sulcus, where the Stria of Gennari (dark line) is clearly visible. b) Normalized histogram of T2* values in ms for gray (red) and white matter (blue) for the 0.37mm^3 data. Dotted lines represent the median. c) ME GRE intensities (left) and estimated T2* values in ms across cortical depths. Panels d-f show the histograms of T2* values in ms for V1 (in yellow) and insulae (yellow) for 10.5T 0.37mm3 data (d); 10.5T 0.8mm3 data (e); and for 7T 0.35mm3 data (f). Dotted lines represent the median.

6 echoes, 4.37 – 26.22; See Methods). Following processing and tissue segmentation, we obtained voxelwise estimates of the quantitative T2* parameters using a nonlinear fitting approach. For visualization of the 10.5T 0.37mm data, these fits were used to perform a weighted average of the data (Figure 5a). This image is artifact free, despite the use of 2D GRAPPA acceleration (R3x3), due to the improvement in acceleration afforded by the higher field strength.

The distributions of gray and white matter T2* values (Figure 5b) were derived from segmentations of the gray and white matter in the 10.5T 0.37 mm data and show high variability across the cortex. Using the gray matter segmentation we examined the T2* estimate as a function of depth within a region around the stria of Gennari. We observe the expected dip (Figure 5c), consistent with the relative increase in myelination along this cortical depth. Even with only 2 runs of the ME-GRE sequence, this effect is visible in both the weighted average (Figure 5c, left panel) as well as the corresponding T2* estimates (Figure 5c right panel).

To further investigate this variability in T2*, we combined our gray matter segmentations with atlas derived measures of the primary visual cortex and the insulae (See Methods). The 0.37mm data at 10.5T (Figure 5e) shows a marked increase in T2* estimates relative to the 0.8mm data at the same field strength (Figure 5d), for both regions. In the visual cortex the gray matter T2* was 21 vs 18 ms for 0.37 and 0.8 mm resolution data, respectively. For the insulae the corresponding numbers were 31 vs 22 ms. The T2* estimates for the 0.8mm data are similar to what is expected based on extrapolations from 9.4T data [60]; however the 0.37mm data suggests that such small voxels experience more homogenous magnetic fields, which may permit acquisitions with extended echo times. The 0.35mm 7T acquisition shows that the 10.5T T2* parameters are approximately 10ms shorter than their 7T counterparts within the same regions at this resolution.

3. DISCUSSION

Submillimeter fMRI allows for non-invasive access to the human brain at the mesoscopic scale, which had previously been the domain of invasive animal model experiments. As discussed in the introduction, such fMRI studies in humans have typically utilized ~0.5μL voxels (e.g. 0.8 mm isotropic dimension), and have been limited by image SNR, fCNR of the functional mapping signals, and brain coverage; as such, they have only been marginally adequate for studying meso-structures such as layers and columns, leading to incorporation of ambitious resolution goals in the US Brain Initiative strategic plan. Here we exploit the higher SNR achievable at 10.5T [48-50] and higher BOLD contrast expected with increasing magnetic fields (e.g. reviews [3,13,61-63] and references therein), in conjunction with high channel count array coils [48-50], NORDIC denoising [54], and tailored reconstructions to overcome the challenges encountered by previous studies.

We demonstrate functional mapping at resolutions that go well beyond the typically employed 0.512μL voxel volume. We recorded functional images with ~0.275μL voxel volumes (0.65 mm isotropic voxels) in cortical regions that are traditionally challenging to image, such as the auditory cortex, located in proximity to air canals and signal drop out regions. We further report functional images in visual cortex with a nominal isotropic resolution of 0.4 mm (0.064μL volume), and 0.35 mm (i.e. 0.0428μL), surpassing the goal set by the BRAIN initiative working group of 0.1μL voxel volume [36,37.] As previously mentioned, the real voxel dimensions typically exceed that of the nominal resolution but are rarely, if ever, reported. The reasons for such blurring include spatial smoothing along one dimension (the phase encode dimension) due to signal decay during the k-space acquisition and post-processing. While pushing to higher nominal resolutions with EPI based acquisitions, it is in fact possible to blur the image so much that the effective resolution starts to decline with increased nominal resolutions [64]. Therefore, in this paper we also provide estimates of the smoothing and demonstrate that at 10.5T, acquisition with nominal resolutions of 0.35 mm isotropic provide resolution gains relative 0.8 and 0.5 mm isotropic (nominal) data at 7T. Finally, we demonstrate the feasibility of submillimeter whole brain fMRI (i.e. 0.75mm

isotropic) with a TR of approximately 3 seconds. These data and their implications are discussed below.

3.1. 0.65 mm fMRI in auditory cortex:

The 0.65 mm resolution (nominal isotropic) auditory fMRI data represents the highest functional images ever achieved in human auditory cortex. Even without tailored reconstructions or denoising, we report high tSNR measures (i.e. ranging between 20 and 30 in grey matter) for a single run (Figure 1c) and statistically significant activation ($p<.05$ FDR corrected) across the auditory cortex with as little as ~38 minutes of data (Figure 1d), including at the single run level (i.e. just over ~7 minutes of data; Figure 1e). These results are even more remarkable considering the location of the auditory cortex relative to regions of increased B_0 inhomogeneities due to susceptibility differences near the air-tissue interface of the ear canals. Such B_0 inhomogeneities can compromise SNR and image quality in EPI based imaging as employed in fMRI and present an increasing challenge with increasing magnetic fields.

We employed a 5/8 partial Fourier acquisition along the phase encode direction to maintain a reasonable TE (i.e. 16.6 ms) and 3D VAT (i.e. ~4.5 seconds). The product partial Fourier reconstruction using zero-padding the section of the k-space data that is not collected is sub-optimal as it results in voxel blurring (visible in Figure 1b) and artificially enhances SNR/tSNR. A popular mathematical algorithm used in many nonparametric reconstruction methods is projection onto convex sets (POCS), which enhances the spatial precision of the reconstructed images (Figure 1b and 1e) at the cost of SNR and related tSNR (Figure 1c). To maximize reconstructed image resolution and SNR, we employed a tailored offline reconstruction pipeline, which includes POCS in conjunction with NORDIC denoising (see Methods). As evidenced by the reconstructed images (Figure 1b) and further demonstrated by the spatial autocorrelation analysis performed on the GLM residuals (Figure 1e), our pipeline significantly ($p<0.05$) decreased spatial blurring in the images without compromising the activation maps (Figure 1d and Figure 1e).

3.2. 0.4 mm isotropic fMRI in visual cortex

0.4 mm isotropic nominal resolution (Figure 2) corresponding to 0.064μL voxels, represents an 8-fold decrease relative to the voxel volumes of 0.8mm isotropic (nominal) data (i.e. 0.512μL volume) that are routinely used for mesoscopic fMRI studies in humans. These images were acquired at 7T and 10.5T in the same participants. We focused on primary visual cortex V1;even within a single run consisting of approximately 5 minutes of data, we can observe statistically significant ($p<.05$ FDR corrected) activation at 10.5T evoked by the visual stimuli in relevant portions of V1 without denoising (Figure 1a). Superior performance of the 10.5T for BOLD fMRI, is demonstrate in this preliminary dataset where approximately four 7T runs (i.e. 4 runs x 5 minutes) were required to achieve a somewhat comparable spatial extent of functional activation realizable with a single 10.5T run (i.e. 5 minutes; Figure 2a); even then, the time course of the voxels considered activated at the t threshold displayed more noise relative the time course of the single run 10.5T data (Figure 2a, right-most panel). The measurable evoked responses to 5 minutes of flickering checkerboards were barely distinguishable from baseline (Figure 2c) and remained so even for ~30 min of data. However, with ~30 min of data, major improvements were observed at 10.5T, with functional maps demonstrating extensive activation encompassing a large portion of the cortical ribbon (Figure 2c).

We further observed that within the retinotopic representation of target and surround, the evoked percent signal change (PSC) to both stimuli was ~2-fold larger at 10.5T compared to 7T (Figure 2b). GRE BOLD fMRI signals can have contributions mediated by microvasculature (capillaries, and small post capillary venules) as well as much larger macrovasculature (i.e. draining veins) (e.g., [13,65]); the extravascular BOLD effect arising from these two distinct contributions display approximately quadratic and linear dependence on B_0, respectively (e.g., [13,65]). The microvascular contribution is intrinsically small but its contribution relative to the larger

macrovascular effect is expected to increase due to their different B_0 dependence. In addition, intrinsically high spatial resolutions, as employed in this paper, are expected to suppress the macrovascular contribution [54,66]. The ~2 fold increase observed in PSC is consistent with this expectation. A purely linear dependence would have yielded only a 1.5-fold increase in PSC and a purely quadratic effect would have yielded a factor of 2.25.

Within the same region where we report PSC differences, we also report a ~2.2 fold increase of t-values for the contrast target and surround > 0. T-values can be approximately conceptualized as PSC over the model standard error, and therefore convey information about the level of unexplained variance and hence the level of noise in the data, albeit not necessarily distinguishing between thermal noise or non-white fluctuations of physiological origin in the fMRI time series; respiration and cardiac pulsation[67-70], and for task/stimulus fMRI, the spatially correlated spontaneous fluctuations ascribed to functional networks in resting state fMRI[71] represent sources of tSNR degradation that are non-white in nature[72-75]. The non-white noise due physiological processes are also B_0 dependent and are expected increase with field strength. Nevertheless, we observe major gains at high resolution 10.5T compared to the 7T even when such noise contributions were not suppressed.

3.3. 0.35 mm isotropic fMRI in visual cortex

As shown by 5 minutes of data (Figure 2), even with 0.4 mm voxels, functional imaging at 10.5T still has reasonable levels of SNR that can be traded in for further increases in spatial resolution. We thus recorded functional images with 0.35mm isotropic (nominal) resolution, 0.0428 μL voxel volume (Figure 3), almost a 12-fold decrease in voxel volume relative to the typical 0.512μL images (e.g. isotropic 0.8mm voxel) and almost 30% smaller than the 0.4mm voxel.

This image resolution, however, remains nominal in nature, as the EPI images are subject to T2* decay and consequential spatial blurring along the phase encode direction, in addition to

the partial Fourier induced resolution losses. However, despite these confounds, as demonstrated by the spatial autocorrelation analyses (Figure 3c), the acquired images at 10.5T exhibit statistically significant ($p<.05$; Bonferroni corrected) *improvements* in resolution relative not only to the 0.8mm but also to the 0.5mm isotropic (nominal) acquired at 7T in the same subject.

At high resolutions, the echo train lengths (*etl*) in EPI sequences gets long and the later echoes can run out of signal thus causing blurring[64] in the phase encode (PE) direction (note that this blurring is only in one dimension). This blurring is similar to the zero-filling of partial Fourier acquisitions but now "zero-filling" occurs on the other end of the k-space in the phase encode dimension due to signal loss in the acquisition. This effect was demonstrated at 7 Tesla for resolutions of $\lesssim$ 0.6 mm isotropic (nominal) when using gradient performance mimicking the Siemens SC72 gradients used at 10.5T at the present. The 2 to 2.5 fold higher SNR over the brain at 10.5T [47-49], however, is an advantage against this type of blurring because even echoes at the end of the echo train can have sufficient signal and SNR. This is expected even though T_2* is somewhat shorter at 10.5T (Figure 5) provided the optimal TE ~T_2* [51] functional contrast is used at each field strength. In addition, as previously mentioned, the *etl* effect on blurring is only on one dimension and we report effective resolutions in all three dimensions

Importantly, after our tailored offline reconstructions, the quality of a single EPI image and the ensuing sensitivity was high enough to allow meaningful functional mapping with as little as 35 minutes of data. As shown in Figure 3c and 3d, the t-maps computed for the contrast target > surround show activation in all expected retinotopic locations. As a further testament of the data quality, single voxel time courses for a single run for target specific voxels (Figure 3e) display the expected temporal hemodynamic characteristics (i.e. peaking during blocks where the target was presented, but not the surround stimulus). We thus proceeded to perform Laminar fMRI analyses by segmenting the cortical ribbon in the retinotopic representation of target and surround in V2 at 11 cortical depths (Figure 3f). After linear detrending, which suppressed the ramping profile associated with the increased responses to larger draining vessels located near the pial surface,

we observed a typical feedback related “pattern of activation” across layers with larger responses in inner and outer depths. These increases in activation in outer and inner depths are also visible as small “bumps” before detrending (Figure 3f). We interpret larger PSC in inner and outer depths as ensuing from top-down spatial attention modulations, which are known to terminate in inner and outer laminae [76]. The subject was instructed to maintain fixation on the fixation dot in the middle of the screen, while focusing on the target (centrally presented) and surround (peripherally presented) stimuli, modulating their spatial attention, and resulting in inner and outer depth modulations in V2.

3.4. 0. 75 mm isotropic resolution whole brain fMRI

The 7T Human Connectome Project (HCP) resting state protocol employed a 1.6mm whole brain acquisition with a TR of 1.0s [57,77], which has been the standard thus far for whole brain task/stimulus or resting state fMRI at 7T. Here, with the high field gains afforded by 10.5T, we propose the next generation of high-resolution whole brain fMRI, one that can achieve sub-millimeter (0.75) resolutions with TRs of 2-3s, while also maintaining sufficient functional sensitivity. We used 2D multi-slice GRE SMS/MB EPI, exploiting combined through plane (i.e. multiband, MB [56]) and in plane accelerations, to decrease TE and TR. Pushing to high resolutions for whole brain studies poses dual challenges of SNR and longer volume acquisition times. The latter is easy to conceptualize in slice-based imaging because the number of slices needed to cover a particular length increases linearly with the reduction in the slice dimension, leading to an increase in the volume acquisition time by the same factor. However, SNR losses due to the smaller voxel volume as well as the longer acquisition times are particularly detrimental fMRI studies where, for example, rapid temporal sampling is needed to accurately capture the small spontaneous resting-state fluctuations in the brain [78]. The combination of 10.5T and high channel coil arrays such as the one used here overcome both of these limitations: 10.5T provides the intrinsic SNR gains that permit high resolutions; in addition, high magnetic fields together high

channel count arrays allow high image acceleration (in this case 12 fold 2D acceleration) (e.g.,[79-81]) thus reducing the image acquisition times to practical levels. Functional mapping at these spatial temporal resolutions and coverage, compatible with resting state whole brain layer resolution fMRI, is an unprecedented opportunity for human neuroscience in single subjects, allowing, in principle, to study connectivity during task and rest across the whole brain, while maintaining the cortical depth sensitivity, which was previously achievable only in local brain regions.

4. CONCLUSION

In conclusion, we present initial results from 10.5T BOLD based fMRI demonstrating functional mapping with high spatiotemporal resolution in partial brain and whole brain imaging. These results were feasible due to the major intrinsic SNR gains available for brain studies at 10.5T, which can be captured using unique high channel count arrays [47-49], and potential for substantial increases in image acceleration without significant amplification of reconstruction noise also enabled by the higher magnetic field of 10.5T and high channel count arrays [47-49]. The results presented usher in the potential gains that will be available in the new era of greater than 10 Tesla human functional imaging, particularly for mesoscale fMRI studies for task/stimulus based designs or HCP style whole brain coverage to capture the spontaneous oscillations in fMRI signals to deduce functional connectivity. Further improvements in effective resolutions as well as temporal sampling (i.e. acceleration) are possible when 10.5T or similarly high, >10T magnetic fields, will be combined with the use of higher performance gradients, and further developments in image acquisition and image reconstruction and denoising strategies.

5. METHODS

1. Experimental paradigms

***1.1. Block design retinotopically organized visual stimulation with flickering gratings**:* The experimental procedure consisted of 12 s on, 12 s off design for the 7T 0.8 mm isotropic voxel acquisitions, and a 24 s on, 24 s off for the 7T 0.5 and 0.4 mm isotropic, and for the 10.5T 0.4 and 0.35 mm isotropic voxel acquisitions. The difference in block length was implemented to account for the difference in volume acquisition time between the 0.8 mm and the other acquisitions (see later). The stimuli consisted of a center (i.e. target) and a surround square checkerboard counterphase flickering (at 6 Hz) gratings subtending approximately 6.5 degrees of visual angle. Stimuli were centered on a background of average luminance (25.4 cd/m^2, 23.5-30.1). Using a Mac Pro computer, stimuli were presented on a Cambridge Research Systems BOLDscreen 32 LCD monitor positioned at the head at 7T (resolution 1920, 1080 at 120 Hz; viewing distance ~89.5 cm.) and using a VPIXX projector at 10.5T (resolution 1920, 1080 at 60 Hz; viewing distance ~89.5 cm.). Stimulus presentation was controlled using Psychophysics Toolbox (3.0.15) based codes. Participants viewed the images through a mirror placed in the head coil.

Each run began and ended with a red fixation dot centered on a gray background and consisted of 3 trials for each of the 2 conditions. This resulted in approximately two and a half minutes runs for the 12 secs on/off (i.e. 0.8 mm 7T) and just over 5 minutes runs for the 24 secs on/off acquisitions. We collected 6 experimental runs per protocol. Participants were instructed to minimize movement and keep fixation locked on the center fixation dot throughout the experimental runs.

***1.2. Block design visual stimulation with objects, bodies and faces**:* The experimental procedure implemented for the whole brain isotropic 0.75 mm acquisition consisted of a

standard 24 s on, 24 s off. The stimuli consisted of a set of face images, bodies without face and objects gratings subtending approximately 5° of visual angle. We equated the amplitude spectrum across all images. Stimuli were centered on a background of average luminance (25.4 cd/m^2, 23.5-30.1). Using Mac Pro computer, stimuli were presented using the VPIXX projector (see above). Stimulus presentation was controlled using Psychophysics Toolbox (3.0.15). Participants viewed the images through a mirror placed in the head coil.

Each run began and ended with black fixation cross centered on a gray background and consisted of 3 trials for each of the 6 conditions. This resulted in approximately 9 minutes runs We collected 4 experimental runs. Participants were instructed to minimize movement and keep fixation locked on the center fixation dot throughout the experimental runs. This experimental paradigm was adapted from [82].

1.3. Auditory stimulation: We adapted the classical local-global paradigm that has been used before to study mismatch negativity (MMN) or 'error-related' responses [83] using cascading sequences. Each trial consisted of a sequence of 4 sounds (100 ms per sound with a 100 ms gap in between) that was presented over a total of 700 ms, followed by a 500 ms gap before the next trial started. The first three sounds were presented in an ascending or descending order with the fourth tone either following this ascending or descending pattern (locally standard trials) or violating this pattern (locally deviant trials). In distinct experimental blocks of 3 minutes each, global regularity was defined according to the presentation rate of each stimulus. Global standard trials were presented 90% of the time, whereas globally rare stimuli were pseudo randomly presented 10% of the time. Four types of trials were created by manipulating local and global regularities: local and global standard, local and global deviant, local standard but global deviant, and local deviant but global standard.

To account for the presentation rate of each frequency, in each block we presented two types of globally standard trials (e.g. frequencies [1 2 3 4] and [2 3 4 5]) that were presented

pseudo-randomly (i.e. they were presented equally often over the span of the whole block and balanced as much as possible in between global deviant trials). In between globally deviant trials (e.g. frequencies [2 3 4 1]), we always presented either 8, 9 or 10 globally standard trials. Each block started with 30 habituation trials (not counted towards the 90%-10% regularity rule) to establish the global regularity before presenting the first globally deviant trial. Each run consisted of two blocks, one in which the globally standard trials were also locally standard (e.g. [1 2 3 4] and [2 3 4 5]) and alternatively one block in which globally standard trials were locally deviant (e.g. [2 3 4 1] and [3 4 5 2]) and the globally deviant trials were locally standard (e.g. [2 3 4 5]). The order of blocks, and the ascending and descending cascades was counterbalanced. Each run lasted approximately 8 minutes and we recorded a total of 8 runs experimental runs.

2. MR Imaging Acquisition and Processing

All 7T functional MRI data were collected with a 7T Siemens Magnetom System with a single transmit and 32-channel receive NOVA head coil for the 0.8mm^3 and the 0.5mm^3 data, and an in-house built 64-channel receive head coil [47,48,50] for the 0.4mm^3 data. All 10.5T MRI data were collected with a 10.5T Siemens Magnetom System with an in-house built 16 transmit and 80 receive -channel head coil [47,48,50]. The in-house developed 10.5T and 7T array coils were extensively characterized in terms of performance [47,48,50].

2.1. 10.5T acquisition protocols: Below we list the acquisition parameters for all protocols:

0.65mm isotropic nominal resolution fMRI: 3D GRE EPI; 0.65 mm isotropic voxels; TE=16.6 ms; TR=81 ms; in-plane acceleration factor along the phase encode direction (iPAT) =4; pF=5/8; 52 Slices; VAT (Volume Acquisition Time)=4536; FOV 272x276mm

0.4 mm isotropic nominal resolution fMRI: 3D GRE EPI ; iPAT=3; 5/8 PF; 40 Slices; TR=113; VAT=4972; TE=24.4

0.35 mm isotropic nominal resolution fMRI: 3D GRE EPI; 0.35 mm iso voxels; iPAT=4; 5/8 PF; 40 Slices; TR=104ms; VAT=5016ms; TE=22.6ms

0.75mm isotropic nominal resolution fMRI: 2D Simultaneous Multi Slice /Multiband (SMS/MB) GRE EPI; TR ~3.2 seconds; iPAT=4; MB3; 5/8 PF; 144 Slices; TR 3210; TE17.8

MP2RAGE Anatomical imaging: 0.7mm isotropic voxels; TR = 5000ms; TE= 1970 ms; Acquisition time: 07:30; FoV=253*270mm; iPAT=4; Inversion 1 = 840 ms; Inversion 2 = 2370 ms; Partial Fourier 6/8

ME GRE acquisition with 0.37 mm isotropic resolution: Whole brain data on two subjects were obtained using parameters TEs: 4.07, 7.95, 11.83, 15.71, 19.59, 23.47, 27.35ms. TR 33ms; FA 10; 7/8ths partial Fourier. GRAPPA: 3x3 Matrix 576x576mm. 320 slices.

ME GRE acquisitions 0.8 mm isotropic resolution: Whole brain data on three subjects were obtained using parameters 0.8mm isotropic resolution, TEs: 4, 8, 12, 16, 20, 24, 28ms. TR 33ms, FA 10. 7/8ths partial Fourier. GRAPPA: 3x2 Matrix 264. 240 slices.

2.2. 7T acquisition protocols.

0.4mm isotropic nominal resolution fMRI: 3D GRE EPI ; iPAT=3; 5/8 PF; 40 Slices; TR=111ms; VAT=4884ms; TE=24.2ms;

0.5mm isotropic nominal resolution fMRI: 3D GE EPI, single slab, 40 slices, TR 83 ms, Volume Acquisition Time (VAT) 3654ms, iPAT 3; 6/8ths Partial Fourier; TE 32.4ms.

0.8mm isotropic nominal resolution fMRI: 2D GE EPI, 40 slices, TR 1350 ms, Multiband factor 2, iPAT 3; 6/8ths Partial Fourier; TE 26.4ms.

ME GRE acquisitions 0.35 mm isotropic resolution: Six acquisitions of 0.35mm isotropic, partial field of view (axial slab, roughly aligned to AC-PC line) multi-echo GRE images were obtained using a 32 Channel NOVA head coil. TEs 4.37, 8.74, 13.11, 17.48, 21.85, 26.22ms. TR 32ms. FA 12 degrees. No partial Fourier. GRAPPA 2x2. Matrix 576 x 576. 160 slices

3. ME GRE data processing for calculation of T2* values

Processing. Due to the bipolar readout, visible distortion was present in odd versus even echoes at 10.5T. To correct for this, we calculated nonlinear alignments, using the SyN appproach between the odd and even echoes (correcting to the intermediate space) using antsRegistration. To align across runs, both Rigid and Nonlinear alignment using the same package was calculated. A final alignment step into the anatomical space from which regions of interest were defined (described below) was also calculated using the same tool. All transforms were combined and applied in a single step to prevent blurring from multiple interpolation steps. Following the transformation, a grand mean was calculated for each echo across the 2 or 3 separate runs.

For the 7T data, distortions were minimal in regions of interest, and therefor nonlinear methods were not used. Instead, the mean of each run was rigidly aligned to the first run and then onward into the anatomical space. Following the transformations, a grand mean was calculated for each echo across the 6 separate runs.

T2* Fits. T2* fits were estimated using the function t2smap from the python package tedana, using the nonlinear curve fitting approach, which is slower but expected to more accurate than the typical log-linear approximation. These T2* estimates were then used to produce a weighted average of the input data.

Regions of Interest. A mask of the gray matter ribbon was produced at high resolution (0.37mm) using the surfaces (smoothwm, pial) derived from FreeSurfer. Labels for white matter and insula areas were derived from the automatic labeling performed by Freesurfer, after upsampling into the 0.37mm space. The label from V1 was produced using the Benson Atlas automated label approach. For GM/WM comparisons a final inclusion mask was manually drawn to include only areas with sufficient signal in the 0.37mm 10.5T data. To produce cortical depths, the high resolution GM ribbon, along with WM and CSF labels was passed through LN2_LAYERS, a part of the LayNii toolbox, using equi-volume depth calculations. The metric file, which contains

a cortical depth estimate for each voxel within the GM, was then used to extract depth dependent metrics from the weighted average and T2* estimates.

4. Functional data Preprocessing

All Functional data preprocessing was performed in BrainVoyager or AFNI. Preprocessing was kept at a minimum and constant across reconstructions. Specifically, we performed slice scan timing corrections for the 2D data only (temporal sinc interpolation), 3D rigid body motion correction (spatial sinc interpolation), where all volumes for all runs were motion corrected relative to the first volume of the first run acquired, and low drift removal (i.e. temporal high pass filtering) using a GLM approach with a design matrix continuing up to the 3rd order discrete cosine transform basis set. No spatial nor temporal smoothing was applied. Functional data were aligned to anatomical data with manual adjustments and iterative optimizations.

EPI data were aligned to T1 weighted images and to T2* ME GRE. For all SMS/MB data sets (i.e. all acquisitions other than the 3D 0.5 mm iso images), anatomical alignment was performed on the Single Band Reference (SBRef) image which was acquired to calibrate coil sensitively profiles prior to the multiband acquisition and has no slice acceleration or T_1-saturation, yielding higher contrast[78].

5. GLMs and tSNR

Stimulus-evoked functional maps were computed in BrainVoyager and in AFNI. Subsequent analyses (i.e. ROI based and statistical testing) were performed in MatLab using a set of tools developed inhouse.

Temporal tSNR was computed by dividing the mean (over time) of the detrended time-courses by its standard deviation independently per voxel, run and subject.

To quantify the extent of stimulus evoked activation, we performed standard general linear model (GLM) estimation (with ordinary least squares minimization). Design matrices (DMs) were

generated by convolution of a double gamma function with a “boxcar” function (representing onset and offset of the stimuli).

5. ROI definition

For the 0.4mm isotropic voxel data sets, we further performed a region of interest (ROI) analyses to compare t values and evoked percent signal changes (PSC) across all voxels within the ROI. The ROI included the retinotopic representation of both target and surround in right V1. The ROI was derived as follows: After co-registering both the 10.5T and the 7T data to the same MP2RAGE, we used run1 (which was excluded from subsequent analyses) to compute the t-contrast target & surround > 0 independently per field strength.

GLM t-values can be approximately conceptualized as beta estimates divided by GLM standard error according to this equation:

$$t = c'b/\sqrt{\mathrm{Var}(e)c'(X'X)^{-1}c} \qquad \text{(eq. 1)}$$

where b represents the beta weights, c is a vector of 1, -1 and 0 indicating the conditions to be contrasted, e is the GLM residuals and X the design matrix. This map (p<.05 uncorrected) was used to define the right hemisphere retinotopic representation of target and surround stimuli within the grey matter boundaries. Finally, the ROI was computed by including all voxels that were found to be significantly active for each of the acquisitions.

6. Quantifying BOLD images Smoothness

Global smoothness estimates were obtained from each reconstruction prior to preprocessing (‘pre’) and following all data preprocessing, just prior to the GLM (‘post’). This was performed using 3dFWHMx from AFNI[84] using the ‘-ACF’ command. The data were detrended using the default settings from 3dFWHMx with the ‘-detrend’ command. As we are interested in the smoothness within the brain, we also used the ‘-automask’ command in order to generate an intensity-based brain mask, based on the median value of each run. This method iterates through

various background clipping parameters to generate a contiguous brain only volume, that excludes the external areas of low signal. The spatial autocorrelation is estimated from the data using a Gaussian plus mono-exponential model, which accounts for possible long-tail spatial autocorrelations found in fMRI data. This estimated FWHM, in mm, from this fitted autocorrelation function is used as an estimate of the smoothness of the data. This estimate was derived for all of the runs, excluding the held-out runs used for ROI creation. For each subject, smoothness was averaged within each stage across the 6 experimental runs to evaluate if global smoothness was markedly increased due to the reconstruction method. Paired sample t-tests were carried out between estimated FWHM parameters to infer statistical significance.

7. Tailored off-line reconstructions

3D GE-EPI reconstruction. The 3D-EPI was obtained with monotonic sampling of the slice-phase encoding direction and preceding each EPI readout a 3-line navigator was acquired without any phase-encoding. Each temporal multi-channel data-sample was decorrelated based on the correlation estimate from a noise-only acquisition. Each EPI readout train was corrected for timing precision using a linear phase obtained from the 3-line navigator, with the same correction applied for all channels. Phase-encoding undersampling was corrected using a two-step GRAPPA implementation, where firstly the missing lines were calculated, and then the acquired data were re-estimated from the neighboring measurements, analogous to a 1-step SPIRIT. Ramp-sampling correction of each readout line was applied using a spline interpolation to the Nyquist sampling. A 1D FFT was applied in the slice-encoding direction. A POCS (projection onto convex sets) partial Fourier reconstruction [53] was applied for each channel and each slice, and the reconstructed images were combined using a SENSE-1 algorithm with ESPIRIT estimated sensitivity profiles. NORDIC denoising was applied to the complex valued time-series as described in [85], where the g-factor and noise were estimated using an implementation of the MPPCA algorithm.

9. Participants

We acquired 7 functional and 2 structural data sets on 3 healthy right-handed subjects (age range: 33-50), with different stimulation paradigms, acquisition parameters and field strengths (see *above*). All subjects had normal, or corrected vision and provided written informed consent. The study complied with all relevant ethical regulations for work with human participants. The local IRB at the University of Minnesota approved the experiments.

6. REFERENCES

1 Ogawa, S., Tank, D. W., Menon, R., Ellermann, J. M., Kim, S. G., Merkle, H. & Ugurbil, K. Intrinsic signal changes accompanying sensory stimulation: functional brain mapping with magnetic resonance imaging. (1992) *Proc Natl Acad Sci U S A* **89**, 5951-5955, **doi**:10.1073/pnas.89.13.5951.

2 Kwong, K. K., Belliveau, J. W., Chesler, D. A., Goldberg, I. E., Weisskoff, R. M., Poncelet, B. P., Kennedy, D. N., Hoppel, B. E., Cohen, M. S., Turner, R., Cheng, H.-M., Brady, T. J. & Rosen, B. R. Dynamic magnetic resonance imaging of human brain activity during primary sensory stimulation. (1992) *Proc Natl Acad Sci U S A* **89**, 5675-5679, **doi**:10.1073/pnas.89.12.5675.

3 Ugurbil, K. Magnetic resonance imaging at ultrahigh fields. (2014) *IEEE Trans Biomed Eng* **61**, 1364-1379, **doi**:10.1109/TBME.2014.2313619.

4 Ugurbil, K. Imaging at ultrahigh magnetic fields: History, challenges, and solutions. (2018) *Neuroimage* **168**, 7-32, **doi**:10.1016/j.neuroimage.2017.07.007.

5 Dumoulin, S. O., Fracasso, A., van der Zwaag, W., Siero, J. C. W. & Petridou, N. Ultra-high field MRI: Advancing systems neuroscience towards mesoscopic human brain function. (2018) *Neuroimage* **168**, 345-357, **doi**:10.1016/j.neuroimage.2017.01.028.

6 De Martino, F., Yacoub, E., Kemper, V., Moerel, M., Uludag, K., De Weerd, P., Ugurbil, K., Goebel, R. & Formisano, E. The impact of ultra-high field MRI on cognitive and computational neuroimaging. (2018) *Neuroimage* **168**, 366-382, **doi**:10.1016/j.neuroimage.2017.03.060.

7 Huber, L., Finn, E. S., Chai, Y., Goebel, R., Stirnberg, R., Stocker, T., Marrett, S., Uludag, K., Kim, S. G., Han, S., Bandettini, P. A. & Poser, B. A. Layer-dependent functional connectivity methods. (2021) *Prog Neurobiol* **207**, 101835, **doi**:10.1016/j.pneurobio.2020.101835.

8 Zaretskaya, N. Zooming-in on higher-level vision: High-resolution fMRI for understanding visual perception and awareness. (2021) *Prog Neurobiol* **207**, 101998, **doi**:10.1016/j.pneurobio.2021.101998.

9 Lawrence, S. J. D., Formisano, E., Muckli, L. & de Lange, F. P. Laminar fMRI: Applications for cognitive neuroscience. (2019) *Neuroimage* **197**, 785-791, **doi**:10.1016/j.neuroimage.2017.07.004.

10 Norris, D. G. & Polimeni, J. R. Laminar (f)MRI: A short history and future prospects. (2019) *Neuroimage* **197**, 643-649, **doi**:10.1016/j.neuroimage.2019.04.082.

11 Polimeni, J. R. & Uludag, K. Neuroimaging with ultra-high field MRI: Present and future. (2018) *Neuroimage* **168**, 1-6, **doi**:10.1016/j.neuroimage.2018.01.072.

12 Weldon, K. B. & Olman, C. A. Forging a path to mesoscopic imaging success with ultra-high field functional magnetic resonance imaging. (2021) *Philos Trans R Soc Lond B Biol Sci* **376**, 20200040, **doi**:10.1098/rstb.2020.0040.

13 Ugurbil, K. What is feasible with imaging human brain function and connectivity using functional magnetic resonance imaging. (2016) *Philos Trans R Soc Lond B Biol Sci* **371**, **doi**:10.1098/rstb.2015.0361.

14 Finn, E. S., Huber, L. & Bandettini, P. A. Higher and deeper: Bringing layer fMRI to association cortex. (2021) *Prog Neurobiol* **207**, 101930, **doi**:10.1016/j.pneurobio.2020.101930.

15 Self, M. W., van Kerkoerle, T., Goebel, R. & Roelfsema, P. R. Benchmarking laminar fMRI: Neuronal spiking and synaptic activity during top-down and bottom-up processing in the different layers of cortex. (2019) *Neuroimage* **197**, 806-817, **doi**:10.1016/j.neuroimage.2017.06.045.

16 Poplawsky, A. J., Fukuda, M. & Kim, S. G. Foundations of layer-specific fMRI and investigations of neurophysiological activity in the laminarized neocortex and olfactory bulb of animal models. (2019) *Neuroimage* **199**, 718-729, **doi**:10.1016/j.neuroimage.2017.05.023.

17 Yacoub, E., Harel, N. & Ugurbil, K. High-field fMRI unveils orientation columns in humans. (2008) *Proc Natl Acad Sci U S A* **105**, 10607-10612, **doi**:10.1073/pnas.0804110105.

18 Santoro, R., Moerel, M., De Martino, F., Goebel, R., Ugurbil, K., Yacoub, E. & Formisano, E. Encoding of natural sounds at multiple spectral and temporal resolutions in the human auditory cortex. (2014) *PLoS Comput Biol* **10**, e1003412, **doi**:10.1371/journal.pcbi.1003412.

19 Cai, Y., Hofstetter, S., van der Zwaag, W., Zuiderbaan, W. & Dumoulin, S. O. Individualized cognitive neuroscience needs 7T: Comparing numerosity maps at 3T and 7T MRI. (2021) *Neuroimage* **237**, 118184, **doi**:10.1016/j.neuroimage.2021.118184.

20 Vu, A. T., Jamison, K., Glasser, M. F., Smith, S. M., Coalson, T., Moeller, S., Auerbach, E. J., Ugurbil, K. & Yacoub, E. Tradeoffs in pushing the spatial resolution of fMRI for the 7T Human Connectome Project. (2017) *Neuroimage* **154**, 23-32, **doi**:10.1016/j.neuroimage.2016.11.049.

21 Schreiber, S., Northall, A., Weber, M., Vielhaber, S. & Kuehn, E. Topographical layer imaging as a tool to track neurodegenerative disease spread in M1. (2021) *Nat Rev Neurosci* **22**, 68-69, **doi**:10.1038/s41583-020-00404-w.

22 McColgan, P., Joubert, J., Tabrizi, S. J. & Rees, G. The human motor cortex microcircuit: insights for neurodegenerative disease. (2020) *Nat Rev Neurosci* **21**, 401-415, **doi**:10.1038/s41583-020-0315-1.

23 Kim, K. X., Dale, C. L., Ranasinghe, K. G., Kothare, H., Beagle, A. J., Lerner, H., Mizuiri, D., Gorno-Tempini, M. L., Vossel, K., Nagarajan, S. S. & Houde, J. F. Impaired Speaking-Induced Suppression in Alzheimer's Disease. (2023) *eNeuro* **10**, **doi**:10.1523/ENEURO.0056-23.2023.

24 Mosconi, M. W., Mohanty, S., Greene, R. K., Cook, E. H., Vaillancourt, D. E. & Sweeney, J. A. Feedforward and feedback motor control abnormalities implicate cerebellar dysfunctions in autism spectrum disorder. (2015) *J Neurosci* **35**, 2015-2025, **doi**:10.1523/JNEUROSCI.2731-14.2015.

25 Sterzer, P., Adams, R. A., Fletcher, P., Frith, C., Lawrie, S. M., Muckli, L., Petrovic, P., Uhlhaas, P., Voss, M. & Corlett, P. R. The Predictive Coding Account of Psychosis. (2018) *Biol Psychiatry* **84**, 634-643, **doi**:10.1016/j.biopsych.2018.05.015.

26 Hardiman, O., Al-Chalabi, A., Chio, A., Corr, E. M., Logroscino, G., Robberecht, W., Shaw, P. J., Simmons, Z. & van den Berg, L. H. Amyotrophic lateral sclerosis. (2017) *Nat Rev Dis Primers* **3**, 17071, **doi**:10.1038/nrdp.2017.71.

27 Kiernan, M. C., Vucic, S., Cheah, B. C., Turner, M. R., Eisen, A., Hardiman, O., Burrell, J. R. & Zoing, M. C. Amyotrophic lateral sclerosis. (2011) *Lancet* **377**, 942-955, **doi**:10.1016/S0140-6736(10)61156-7.

28 Ugurbil, K. *et al*. Pushing spatial and temporal resolution for functional and diffusion MRI in the Human Connectome Project. (2013) *Neuroimage* **80**, 80-104, **doi**:10.1016/j.neuroimage.2013.05.012.

29 Glasser, M. F. *et al*. The Human Connectome Project's neuroimaging approach. (2016) *Nat Neurosci* **19**, 1175-1187, **doi**:10.1038/nn.4361.

30 Van Essen, D. C., Smith, S. M., Barch, D. M., Behrens, T. E., Yacoub, E., Ugurbil, K. & Consortium, W. U.-M. H. The WU-Minn Human Connectome Project: an overview. (2013) *Neuroimage* **80**, 62-79, **doi**:10.1016/j.neuroimage.2013.05.041.

31 Van Essen, D. C. & Ugurbil, K. The future of the human connectome. (2012) *Neuroimage* **62**, 1299-1310, **doi**:10.1016/j.neuroimage.2012.01.032.

32 Elam, J. S. *et al*. The Human Connectome Project: A retrospective. (2021) *Neuroimage* **244**, 118543, **doi**:10.1016/j.neuroimage.2021.118543.

33 Beckett, A. J. S., Dadakova, T., Townsend, J., Huber, L., Park, S. & Feinberg, D. A. Comparison of BOLD and CBV using 3D EPI and 3D GRASE for cortical layer functional MRI at 7 T. (2020) *Magn Reson Med* **84**, 3128-3145, **doi**:10.1002/mrm.28347.

34 Huber, L., Handwerker, D. A., Jangraw, D. C., Chen, G., Hall, A., Stuber, C., Gonzalez-Castillo, J., Ivanov, D., Marrett, S., Guidi, M., Goense, J., Poser, B. A. & Bandettini, P. A. High-Resolution CBV-fMRI Allows Mapping of Laminar Activity and Connectivity of Cortical Input and Output in Human M1. (2017) *Neuron* **96**, 1253-1263 e1257, **doi**:10.1016/j.neuron.2017.11.005.

35 Zimmermann, J., Goebel, R., De Martino, F., van de Moortele, P. F., Feinberg, D., Adriany, G., Chaimow, D., Shmuel, A., Ugurbil, K. & Yacoub, E. Mapping the organization of axis of motion selective features in human area MT using high-field fMRI. (2011) *PLoS One* **6**, e28716, **doi**:10.1371/journal.pone.0028716.

36 *BRAIN 2025: A Scientific Vision (BRAIN 1.0)*, <https://braininitiative.nih.gov/sites/default/files/pdfs/brain2025_508c.pdf> (2014).

37 Jorgenson, L. A. *et al*. The BRAIN Initiative: developing technology to catalyse neuroscience discovery. (2015) *Philos Trans R Soc Lond B Biol Sci* **370**, **doi**:10.1098/rstb.2014.0164.

38 *BRAIN Initiave 2.0: From Cells to Circuits, Toward Cures (BRAIN 2.0)*, <https://braininitiative.nih.gov/sites/default/files/images/brain_2.0_6-6-19-final_revised10302019_508c.pdf> (2019).

39 Eisenstein, M. Pushing the limits of MRI brain imaging. (2024) *Nature Methods* **21**, 1975-1979, **doi**:10.1038/s41592-024-02489-y.

40 Nowogrodzki, A. The world's strongest MRI machines are pushing human imaging to new limits. (2018) *Nature* **563**, 24-26.

41 Ugurbil, K., Van de Moortele, P. F., Grant, A., Auerbach, E. J., Erturk, A., Lagore, R., Ellermann, J. M., He, X., Adriany, G. & Metzger, G. J. Progress in Imaging the Human Torso at the Ultrahigh Fields of 7 and 10.5 T. (2021) *Magn Reson Imaging Clin N Am* **29**, e1-e19, **doi**:10.1016/j.mric.2020.10.001.

42 Sadeghi-Tarakameh, A., DelaBarre, L., Lagore, R. L., Torrado-Carvajal, A., Wu, X., Grant, A., Adriany, G., Metzger, G. J., Van de Moortele, P. F., Ugurbil, K., Atalar, E. & Eryaman, Y. In vivo human head MRI at 10.5T: A radiofrequency safety study and preliminary imaging results. (2020) *Magn Reson Med* **84**, 484-496, **doi**:10.1002/mrm.28093.

43 He, X., Erturk, M. A., Grant, A., Wu, X., Lagore, R. L., DelaBarre, L., Eryaman, Y., Adriany, G., Auerbach, E. J., Van de Moortele, P. F., Ugurbil, K. & Metzger, G. J. First in-vivo human imaging at 10.5T: Imaging the body at 447 MHz. (2020) *Magn Reson Med* **84**, 289-303, **doi**:10.1002/mrm.28131.

44 Grant, A., Metzger, G. J., Van de Moortele, P. F., Adriany, G., Olman, C., Zhang, L., Koopermeiners, J., Eryaman, Y., Koeritzer, M., Adams, M. E., Henry, T. R. & Ugurbil, K. 10.5 T MRI static field effects on human cognitive, vestibular, and physiological function. (2020) *Magn Reson Imaging* **73**, 163-176, **doi**:10.1016/j.mri.2020.08.004.

45 Schmidt, S., Erturk, M. A., He, X., Haluptzok, T., Eryaman, Y. & Metzger, G. J. Improved (1) H body imaging at 10.5 T: Validation and VOP-enabled imaging in vivo with a 16-channel transceiver dipole array. (2024) *Magn Reson Med* **91**, 513-529, **doi**:10.1002/mrm.29866.

46 Le Ster, C., Grant, A., Van de Moortele, P. F., Monreal-Madrigal, A., Adriany, G., Vignaud, A., Mauconduit, F., Rabrait-Lerman, C., Poser, B. A., Ugurbil, K. & Boulant, N. Magnetic field strength dependent SNR gain at the center of a spherical phantom and up to 11.7T. (2022) *Magn Reson Med* **88**, 2131-2138, **doi**:10.1002/mrm.29391.

47 Zhang, B., Radder, J., Giannakopoulos, I., Grant, A., Lagore, R., Waks, M., Tavaf, N., Van de Moortele, P. F., Adriany, G., Sadeghi-Tarakameh, A., Eryaman, Y., Lattanzi, R. & Ugurbil, K. Performance of receive head arrays versus ultimate intrinsic SNR at 7 T and 10.5 T. (2024) *Magn Reson Med* **92**, 1219-1231, **doi**:10.1002/mrm.30108.

48 Waks, M. *et al.* RF coil design strategies for improving SNR at the ultrahigh magnetic field of 10.5T. (2025) *Magn Reson Med* **93**, 873-888, **doi**:10.1002/mrm.30315.

49 Lagore, R. L. *et al.* A 128 Receive array with enhanced SNR Performance for 10.5 Tesla Brain Imaging. (2024) *bioRxiv*, **doi**:10.1101/2024.10.20.619294.

50 Waks, M. *et al.* RF coil design strategies for improving SNR at the ultrahigh magnetic field of 10.5 Tesla. (2024) *bioRxiv*, **doi**:10.1101/2024.05.23.595628.

51 Blamire, A. M., Ogawa, S., Ugurbil, K., Rothman, D., McCarthy, G., Ellermann, J. M., Hyder, F., Rattner, Z. & Shulman, R. G. Dynamic mapping of the human visual cortex by high-speed magnetic resonance imaging. (1992) *Proc Natl Acad Sci U S A* **89**, 11069-11073, **doi**:10.1073/pnas.89.22.11069.

52 Menon, R. S., Ogawa, S., Tank, D. W. & Ugurbil, K. Tesla gradient recalled echo characteristics of photic stimulation-induced signal changes in the human primary visual cortex. (1993) *Magn Reson Med* **30**, 380-386, **doi**:10.1002/mrm.1910300317.

53 Cuppen, J. & van Est, A. Reducing MR imaging time by one-sided reconstruction. (1987) *Magn Reson Imaging* **5**, 526-527, **doi**:https://doi.org/10.1016/0730-725X(87)90402-4.

54 Vizioli, L., Moeller, S., Dowdle, L., Akcakaya, M., De Martino, F., Yacoub, E. & Ugurbil, K. Lowering the thermal noise barrier in functional brain mapping with magnetic resonance imaging. (2021) *Nat Commun* **12**, 5181, **doi**:10.1038/s41467-021-25431-8.

55 Cox, R. W., Chen, G., Glen, D. R., Reynolds, R. C. & Taylor, P. A. FMRI Clustering in AFNI: False-Positive Rates Redux. (2017) *Brain Connect* **7**, 152-171, **doi**:10.1089/brain.2016.0475.

56 Moeller, S., Yacoub, E., Olman, C. A., Auerbach, E., Strupp, J., Harel, N. & Ugurbil, K. Multiband multislice GE-EPI at 7 tesla, with 16-fold acceleration using partial parallel imaging with application to high spatial and temporal whole-brain fMRI. (2010) *Magn Reson Med* **63**, 1144-1153, **doi**:10.1002/mrm.22361.

57 Ugurbil, K. *et al*. Pushing spatial and temporal resolution for functional and diffusion MRI in the Human Connectome Project. (2013) *Neuroimage* **80**, 80-104, **doi**:10.1016/j.neuroimage.2013.05.012.

58 Setsompop, K., Gagoski, B. A., Polimeni, J. R., Witzel, T., Wedeen, V. J. & Wald, L. L. Blipped-controlled aliasing in parallel imaging for simultaneous multislice echo planar imaging with reduced g-factor penalty. (2012) *Magn Reson Med* **67**, 1210-1224, **doi**:10.1002/mrm.23097.

59 Marques, J. P., Kober, T., Krueger, G., van der Zwaag, W., Van de Moortele, P. F. & Gruetter, R. MP2RAGE, a self bias-field corrected sequence for improved segmentation and T1-mapping at high field. (2010) *Neuroimage* **49**, 1271-1281, **doi**:10.1016/j.neuroimage.2009.10.002.

60 Pohmann, R., Speck, O. & Scheffler, K. Signal-to-noise ratio and MR tissue parameters in human brain imaging at 3, 7, and 9.4 tesla using current receive coil arrays. (2016) *Magn Reson Med* **75**, 801-809, **doi**:10.1002/mrm.25677.

61 Uludag, K. & Blinder, P. Linking brain vascular physiology to hemodynamic response in ultra-high field MRI. (2018) *Neuroimage* **168**, 279-295, **doi**:10.1016/j.neuroimage.2017.02.063.

62 Uludag, K. & Ugurbil, K. in *fMRI: From Nuclear Spins to Brain Function Biological Magnetic Resonance* (eds K. Uludag, K. Ugurbil, & L. Berliner) Ch. 8, 163-214 (Springer, 2015).

63 Uludag, K., Muller-Bierl, B. & Ugurbil, K. An integrative model for neuronal activity-induced signal changes for gradient and spin echo functional imaging. (2009) *Neuroimage* **48**, 150-165, **doi**:10.1016/j.neuroimage.2009.05.051.

64 Feinberg, D. A. *et al*. Next-generation MRI scanner designed for ultra-high-resolution human brain imaging at 7 Tesla. (2023) *Nat Methods* **20**, 2048-2057, **doi**:10.1038/s41592-023-02068-7.

65 Ogawa, S., Menon, R. S., Tank, D. W., Kim, S. G., Merkle, H., Ellermann, J. M. & Ugurbil, K. Functional brain mapping by blood oxygenation level-dependent contrast magnetic resonance imaging. A comparison of signal characteristics with a biophysical model. (1993) *Biophys J* **64**, 803-812, **doi**:10.1016/S0006-3495(93)81441-3.

66 Ugurbil, K. ULTRAHIGH FIELD and ULTRAHIGH RESOLUTION fMRI. (2021) *Curr Opin Biomed Eng* **18**, **doi**:10.1016/j.cobme.2021.100288.

67 Hu, X. & Kim, S. G. Reduction of signal fluctuation in functional MRI using navigator echoes. (1994) *Magn Reson Med* **31**, 495-503, **doi**:10.1002/mrm.1910310505.

68 Bianciardi, M., Fukunaga, M., van Gelderen, P., Horovitz, S. G., de Zwart, J. A., Shmueli, K. & Duyn, J. H. Sources of functional magnetic resonance imaging signal fluctuations in the human brain at rest: a 7 T study. (2009) *Magn Reson Imaging* **27**, 1019-1029, **doi**:10.1016/j.mri.2009.02.004.

69 Bianciardi, M., van Gelderen, P., Duyn, J. H., Fukunaga, M. & de Zwart, J. A. Making the most of fMRI at 7 T by suppressing spontaneous signal fluctuations. (2009) *Neuroimage* **44**, 448-454, **doi**:10.1016/j.neuroimage.2008.08.037.

70 Fox, M. D., Snyder, A. Z., Zacks, J. M. & Raichle, M. E. Coherent spontaneous activity accounts for trial-to-trial variability in human evoked brain responses. (2006) *Nature neuroscience* **9**, 23-25, **doi**:10.1038/nn1616.

71 Smith, S. M., Fox, P. T., Miller, K. L., Glahn, D. C., Fox, P. M., Mackay, C. E., Filippini, N., Watkins, K. E., Toro, R., Laird, A. R. & Beckmann, C. F. Correspondence of the brain's functional architecture during activation and rest. (2009) *Proc Natl Acad Sci U S A* **106**, 13040-13045, **doi**:10.1073/pnas.0905267106.

72 Kay, K. N., Rokem, A., Winawer, J., Dougherty, R. F. & Wandell, B. A. GLMdenoise: a fast, automated technique for denoising task-based fMRI data. (2013) *Front Neurosci* **7**, 247, **doi**:10.3389/fnins.2013.00247.

73 Caballero-Gaudes, C. & Reynolds, R. C. Methods for cleaning the BOLD fMRI signal. (2017) *Neuroimage* **154**, 128-149, **doi**:10.1016/j.neuroimage.2016.12.018.

74 Lund, T. E., Madsen, K. H., Sidaros, K., Luo, W. L. & Nichols, T. E. Non-white noise in fMRI: does modelling have an impact? (2006) *Neuroimage* **29**, 54-66, **doi**:10.1016/j.neuroimage.2005.07.005.

75 Murphy, K., Birn, R. M. & Bandettini, P. A. Resting-state fMRI confounds and cleanup. (2013) *Neuroimage* **80**, 349-359, **doi**:10.1016/j.neuroimage.2013.04.001.

76 Vizioli, L., Huber, L. & Yacoub, E. in *Ultra-high field neuro MRI* (eds Maxime Guye, Karin Markenroth Bloch, & Benedikt A. Poser) (2023).

77 Sotiropoulos, S. N. *et al*. Advances in diffusion MRI acquisition and processing in the Human Connectome Project. (2013) *Neuroimage* **80**, 125-143, **doi**:10.1016/j.neuroimage.2013.05.057.

78 Smith, S. M. *et al*. Resting-state fMRI in the Human Connectome Project. (2013) *Neuroimage* **80**, 144-168, **doi**:10.1016/j.neuroimage.2013.05.039.

79 Ohliger, M. A., Grant, A. K. & Sodickson, D. K. Ultimate intrinsic signal-to-noise ratio for parallel MRI: electromagnetic field considerations. (2003) *Magn Reson Med* **50**, 1018-1030, **doi**:10.1002/mrm.10597.

80 Wiesinger, F., Van de Moortele, P. F., Adriany, G., De Zanche, N., Ugurbil, K. & Pruessmann, K. P. Potential and feasibility of parallel MRI at high field. (2006) *NMR Biomed* **19**, 368-378, **doi**:10.1002/nbm.1050.

81 Wiesinger, F., Van de Moortele, P. F., Adriany, G., De Zanche, N., Ugurbil, K. & Pruessmann, K. P. Parallel imaging performance as a function of field strength--an experimental investigation using electrodynamic scaling. (2004) *Magn Reson Med* **52**, 953-964, **doi**:10.1002/mrm.20281.

82 Stigliani, A., Weiner, K. S. & Grill-Spector, K. Temporal Processing Capacity in High-Level Visual Cortex Is Domain Specific. (2015) *J Neurosci* **35**, 12412-12424, **doi**:10.1523/JNEUROSCI.4822-14.2015.

83 Bekinschtein, T. A., Dehaene, S., Rohaut, B., Tadel, F., Cohen, L. & Naccache, L. Neural signature of the conscious processing of auditory regularities. (2009) *Proc Natl Acad Sci U S A* **106**, 1672-1677, **doi**:10.1073/pnas.0809667106.

84 Cox, R. W. AFNI: software for analysis and visualization of functional magnetic resonance neuroimages. (1996) *Comput Biomed Res* **29**, 162-173, **doi**:10.1006/cbmr.1996.0014.

85 Moeller, S., Pisharady, P. K., Ramanna, S., Lenglet, C., Wu, X., Dowdle, L., Yacoub, E., Ugurbil, K. & Akcakaya, M. NOise reduction with DIstribution Corrected (NORDIC) PCA in dMRI with complex-valued parameter-free locally low-rank processing. (2021) *Neuroimage* **226**, 117539, **doi**:10.1016/j.neuroimage.2020.117539.